A 1.4-GHz GaAs MMIC Radiometer for Noninvasive Internal Body Thermometry

Jooeun Lee, *Graduate Student Member, IEEE*, Gabriel Santamaria Botello, *Member, IEEE*, Robert Streeter, *Member, IEEE*, and Zoya Popović, *Fellow, IEEE*

***Abstract*— In this article, we present an on-chip Dicke radiometer for noninvasive internal body temperature measurements. The switch and low-noise high-gain amplifier are implemented in a 0.1-μm enhancement-mode pseudomorphic high-electron-mobility transistor (pHEMT) GaAs process. The single-pole double-throw (SPDT) switch in a series-shunt topology with a resonating inductor shows an insertion loss of 0.29 dB and an isolation of 30.8 dB at 1.4 GHz. The low-noise amplifier (LNA) has a measured stable gain of 45.2 dB and a noise figure of 0.52 dB. Following the gain path, two bandpass filters with a 64-MHz power-equivalent bandwidth centered at 1.4 GHz help reduce electromagnetic interference. The monolithic microwave integrated circuit (MMIC) of the radiometer shows 45 dB of gain and 0.88-dB noise figure at 1.4 GHz. When connected to a near-field antenna probe, measurements are obtained on a skin–muscle phantom to track the muscle temperature. The near-field antenna is designed to receive blackbody radiation from a 15-mm-thick muscle phantom under a 2-mm-thick skin phantom. To retrieve the subcutaneous temperature of the muscle, the calibrated radiometer measures total noise power with an integration time of 2 s. Compared to a thermocouple measurement performed 30 s before the radiometric measurement, an average error of 0.77 K is obtained. In vivo thermometry of water inside a human cheek is performed for validation, and the impact of varying skin properties on temperature estimation is studied in simulations.**

***Index Terms*— Detector, GaAs monolithic microwave integrated circuit (MMIC), low-noise amplifier (LNA), microwave thermometry, radiometer, RF switch, thermal noise.**

I. Introduction

THE acquisition and long-term monitoring of internal tissue temperature is a valuable metric with benefits across the medical space. For instance, artificial hypothermia is needed for emergency cardiac repair surgery, during which the blood supply is interrupted. However, a smooth return to normothermia is required within only 30 min to avoid brain damage. Throughout this procedure, the brain temperature is typically monitored with a proximal nasal catheter [1], which does not give an accurate measurement of the brain temperature. Another case where internal temperature measurements are useful is the monitoring of muscle temperature in first responders, athletes, and military personnel, which can help prevent heat-related injuries and optimize athletic performance [2], [3]. Furthermore, the diagnosis of sleep disorders is related to body core temperature [4] and tracking internal temperature can inform external modifiers for sleep disorder treatment. Internal tissue temperature is also an indicator of infection, joint inflammation [5], and burn healing [6]. In addition to diagnostics, therapeutic methods, such as cancer hyperthermia, e.g., [7], can critically benefit from internal tissue temperature monitoring.

Currently, there is no commercially available wearable device that can noninvasively measure temperature at a few centimeters depth in the body. Invasive methods include needle probes and radio pills, while noninvasive indirect relative MRI high-resolution temperature mapping is large and expensive [8]. Heat-flux devices have been demonstrated in clinical settings [9]. However, this method detects the temperature at a limited depth below the skin. More recently, heat-flux sensors have been used in wearable form, focusing on exercise monitoring [10]. In this article, we focus on microwave radiometry for internal tissue thermometry. The approach is shown in Fig. 1, where a near-field antenna attached to the outer skin receives thermal power from a stack of tissue layers. The very low received power (tens of femtowatts) is amplified and detected by a Dicke radiometer. A separate thermocouple on the skin allows estimation of the temperature of the inner tissue layers.

The power spectral density, p, of thermal radiation can be approximated as white noise in the microwave frequency range

$$p = \frac{hf}{e^{\frac{hf}{kT}} - 1} \approx kT \quad \text{for} \quad f \ll kT/h \tag{1}$$

where h and k are Plank's and Boltzmann's constants, f is the frequency, and T is the temperature in kelvin. For normal human body temperature around 310 K, the blackbody curve peaks in the infrared frequency range at approximately 18 THz. However, at this frequency, the penetration

Manuscript received 10 July 2023; revised 8 September 2023; accepted 3 October 2023. Date of publication 16 October 2023; date of current version 10 January 2024. The work of Jooeun Lee was supported by the National Science Foundation under Award IIP 2044668. The work of Robert Streeter was supported by the National Science Foundation under Award ECCS 2026523. *(Corresponding author: Jooeun Lee.)*

Jooeun Lee, Robert Streeter, and Zoya Popović are with the Department of Electrical, Computer, and Energy Engineering, University of Colorado at Boulder, Boulder, CO 30309 USA (e-mail: jooeun.lee@colorado.edu; robert.streeter@colorado.edu; zoya.popovic@colorado.edu).

Gabriel Santamaria Botello was with the Department of Electrical, Computer, and Energy Engineering, University of Colorado at Boulder, Boulder, CO 30309 USA. He is now with the Department of Electrical Engineering, Colorado School of Mines, Golden, CO 80401 USA (e-mail: gabriel.santamariabotello@mines.edu).

Color versions of one or more figures in this article are available at https://doi.org/10.1109/TMTT.2023.3322859.

Digital Object Identifier 10.1109/TMTT.2023.3322859

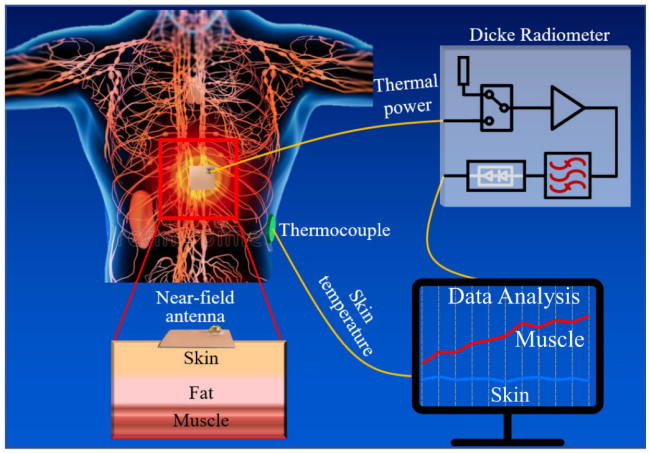

Fig. 1. Illustration of noninvasive internal body thermometry with a microwave radiometer placed below the sternum [11]. A near-field antenna is placed on the skin to receive thermal power from a stack of tissue layers. This signal is transferred to a low-noise receiver, and the output is processed with a temperature estimation algorithm. A thermocouple on the skin provides additional information to the algorithm.

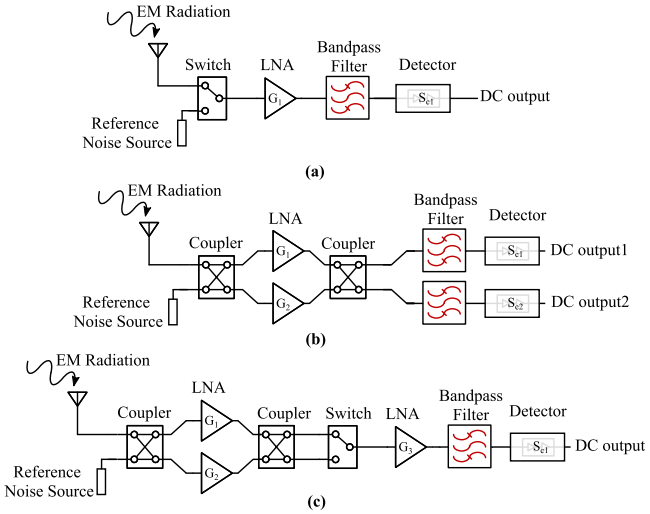

Fig. 2. Diagrams of different radiometer architectures: (a) Dicke, (b) correlation, and (c) hybrid radiometers.

of electromagnetic waves in most tissues is very small (on the order of millimeters). Therefore, infrared measurements can only give skin temperature. We refer to the depth at which temperature can be measured as "sensing depth." To receive power from subsurface tissue layers, a lower microwave frequency of around 1.4 GHz is used as a compromise between sensing depth and size of the thermometer components, especially the filters and the near-field antenna placed on the skin.

Although a heterodyne receiver can also be used to detect thermal radiations, the radiometer approach is simpler and potentially has lower power consumption. Microwave radiometry for internal tissue measurements has been demonstrated in the literature over the past few decades, e.g., with a 0.9–1.2-GHz Dicke radiometer with a matched loop antenna placed on the stomach, Enander and Larson [12] measured a 1.5 °C temperature change when drinking cold water. A 45-GHz radiometer with a horn antenna was used to obtain temperature body images that were reported to show the heart location in [13]. In [14], a multifrequency Dicke radiometer at 1.5, 2.5, and 3.5 GHz was used to differentiate surface and subsurface temperature. A 1.4-GHz Dicke radiometer with off-the-shelf components, a power consumption of around 0.6 W, and a noise figure of 1.58 dB was demonstrated in [15] to measure the temperature of a muscle tissue phantom under the skin and fat layers with as low as 0.2 K resolution. More recently, a 3.4–4.2-GHz Dicke radiometer with a circulator for reflection coefficient fluctuation reduction and with a power consumption of 1.05 W is shown in [16], with applications such as breast cancer detection and back pain assessment.

Previously published radiometers were implemented from off-the-shelf components, resulting in a size not smaller than about 3 × 3 cm. With the goal of reducing the size of the radiometer as well as its power consumption, the approach taken in this article is to monolithically integrate several radiometer components. This can enable a wearable low-power device that is less susceptible to interference. The results in this article expand on the research presented at the IEEE International Microwave Symposium 2023, San Diego [17]. Section II gives an overview of radiometer architecture tradeoffs and the main parameters that motivate the choice of the Dicke architecture for integration on a GaAs pseudomorphic high-electron-mobility transistor (pHEMT) monolithic microwave integrated circuit (MMIC). Section III describes the design and characterization of the near-field antenna that receives thermal radiation from the skin and subcutaneous tissue layers. Section IV presents the design and measurements of the MMIC radiometer switch and low-noise amplifier (LNA) components. Section V gives details on radiometer implementation and characterization. Section VI presents the new results for radiometry measurements and temperature estimation in several scenarios: two phantom stacks and in vivo on a human cheek. The phantom measurements are performed for temperatures above and below room temperature for up to 45 min and show promising results with average errors of 0.1 and 0.31 K, respectively. Finally, Section VII discusses the simulation results that quantify the sensitivity of temperature estimation to tissue layer properties and summarizes the results of this article.

II. Radiometer Overview

A key metric for radiometer performance is the minimal detectable temperature difference, ΔT, which depends on the system noise temperature T_{sys}, measurement bandwidth B, and integration time τ. Several radiometer architectures, shown in Fig. 2, can be compared in terms of this metric to point to tradeoffs for any given application. For the simplest total power radiometer, which consists of an LNA, filter, and detector [18], the temperature resolution, or sensitivity, is given by

$$\Delta T = \frac{T_{\text{sys}}}{\sqrt{\tau B}} \tag{2}$$

and is susceptible to drift and fluctuations, which cannot be calibrated during operation.

TABLE I
COMPARISON OF RADIOMETER ARCHITECTURES

	Dicke [16]	**Correlation [21]**	**Hybrid [20]**
ΔT	$2T_{sys}/\sqrt{\tau B}$	$\sqrt{2}T_{sys}/\sqrt{\tau B}$	$2T_{sys}/\sqrt{\tau B}$
Pros	– Gain fluctuation calibrated	– No switch loss (but coupler loss) -100% duty cycle	– No switch loss (but coupler loss) – Gain flucturation calibrated
Cons	– Sensitive to input impedance – Limited time on target	– Duplicate components – Sensitive to phase balance	– Duplicate components – Limited time on target

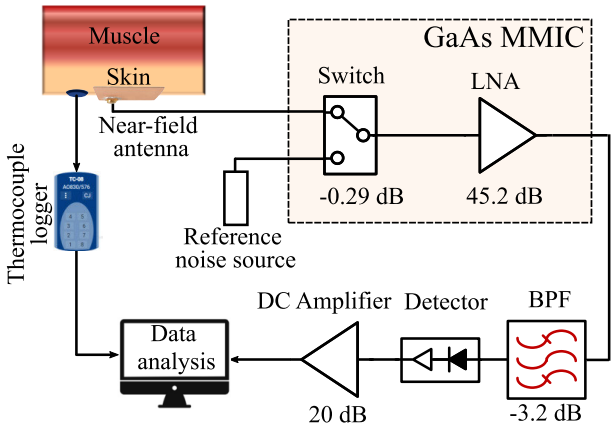

Fig. 3. Block diagram of a Dicke radiometer connected to a phantom tissue stack of skin and muscle. The Dicke switch and LNA are implemented on a GaAs MMIC and followed by off-chip bandpass filter, detector, and dc amplifier. The output is digitized and processed for temperature retrieval. A thermocouple logger monitors skin temperature.

Other radiometer architectures include the Dicke radiometer, correlation radiometer, and a combination of the two, which we refer to as the "hybrid radiometer." A Dicke radiometer uses a switch after the antenna for calibrating gain fluctuations of all components that follow. This is performed by comparing to a known thermal source at the expense of a commonly chosen 50% duty cycle of the measurement, which reduces the total received power from the target [18]. However, the loss of the switch increases T_{sys}.

The correlation radiometer has a balanced hybrid coupler with two low-noise gain paths, with the advantage of continuous measurement of both the target and reference. In addition, the coupler makes this design less sensitive to impedance mismatches at the inputs since the output noise signal is only affected by the reflection of the source input and independent of the phase [19]. However, this structure is sensitive to gain fluctuation in the detector stage due to the two separate paths. For the hybrid topology [20], the switch is placed after the hybrid couplers. This architecture is robust to load impedance variations, and the switch also reduces sensitivity to gain fluctuations of components that follow it. Besides reducing the overall uncertainty, the hybrid radiometer is ideally balanced, meaning that the voltage difference between outputs is zero. This further reduces the uncertainty from the flicker noise of the components before the switch. Table I shows a summary of the achievable ΔT, as well as the pros and cons of various architectures. In this article, we show an implementation of a Dicke architecture, chosen due to its simplicity and the fact that human temperature changes on a scale much slower than the required switching period.

Fig. 3 shows the block diagram of the Dicke radiometer. A near-field antenna is designed to effectively receive blackbody radiation from a buried tissue layer. It couples the total radiometric power received from all tissue layers to a switch that alternates between the tissue stack and a known noise reference. This allows calibration for slow-varying gain fluctuations. The LNA gain is selected to meet a gain budget and is followed by broadband and narrowband bandpass filters. The detector converts the amplified thermal noise input to a dc voltage. At the output of the postdetection amplifier, the voltage from a room-temperature source is on the order of 10 mV. After considering the detector responsivity, loss in the filters, switch loss, and cable loss, as well as near-field antenna mismatch, a requirement for the LNA gain is found to be >45 dB, assuming a room-temperature input power of −100 dBm in the 1.4-GHz quiet radio astronomy band. The overall receiver noise figure is primarily determined by the first-stage LNA noise figure and loss of the switch. The design of the radiometer components is discussed next.

III. NEAR-FIELD ANTENNA DESIGN

To receive blackbody radiation from a subcutaneous tissue layer, a near-field antenna different from a free-space radiator is designed. The goals for the design include small size for wearability, combined with spatial resolution in the lateral dimension and sensing depth in the vertical direction (see Fig. 3). Previously published works have used, e.g., slot [15], bow-tie [22], and waveguide [23] topologies, with more examples given in [24]. A rectangular patch topology is selected for simplicity because the ground plane reduces back lobes that can receive interference. The goal, in this case, is to receive as much power as possible from the muscle layer under the skin layer. A 2-mm skin phantom ($\epsilon_r = 28$ and $\sigma = 0.82$ S/m) from [25] is placed on top of a plastic bag filled with saline solution ($\epsilon_r = 77.7$ and $\sigma = 1.26$ S/m) used as a muscle phantom, approximating the values given in [26]. The muscle phantom is kept in a water bath with a temperature controller that sets the temperature to a known value for characterizing radiometer accuracy.

A coaxial-fed rectangular patch is designed by simulation in Ansys HFSS. The x and y dimensions of the tissue phantom layers are 6 × 6 cm, surrounded by air. A 1.27-mm-thick Rogers RO3010 material is used for the substrate and superstrate, with dimensions shown in Fig. 4. The Rogers RO3010 substrate has a high permittivity of $\epsilon_r = 10.2$, which reduces the size of the near-field antenna. The superstrate placed on top of the rectangular patch allows deeper penetration depth by acting as an intermediate matching layer as well as focusing the near-field coupling. The superstrate also reduces the sensitivity of return loss to different tissue layers. The resulting size of the rectangular metal patch is 42 × 40 mm for operation at 1.4 GHz. The simulated and measured reflection

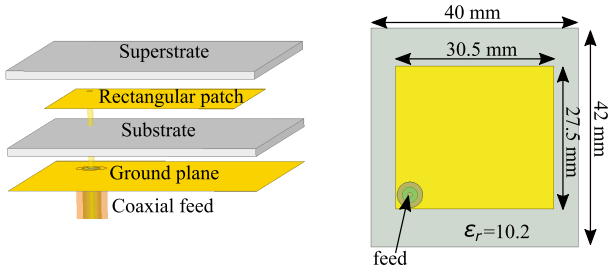

Fig. 4. Cross section of the near-field antenna designed for thermal power retrieval, with a high sensing coefficient from the muscle phantom layer (left) and top view of the near-field antenna with detailed parameters (right).

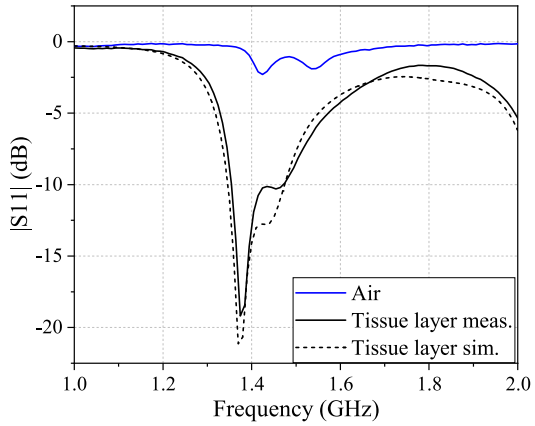

Fig. 5. Simulated and measured reflection coefficient magnitude when the near-field antenna is placed onto the phantom tissue stack. The measured reflection coefficient is also shown for the antenna in free space for comparison.

coefficient magnitudes are shown in Fig. 5. The comparison with the antenna measured in air clearly shows that it is designed to be matched to a specific tissue stack.

The total thermal power received by the near-field antenna is a weighted sum of the powers from different tissues, and therefore, the equivalent total temperature that is measured by the radiometer can be written as

$$T = \sum_{i=1}^{N} W_i \cdot T_i \tag{3}$$

where T_i is the temperature of the ith layer and W_i is the corresponding weighting factor, which can be determined from full-wave electromagnetic simulations, described in Section VI. To estimate the temperature of a buried tissue layer, the weights W_i are determined by calculating the percentage of power dissipated in the ith tissue layer relative to the total power delivered to the tissue stack when the probe transmitting and using reciprocity as in [15]. An example is shown in Fig. 6 for the probe design from Fig. 4 and the skin–muscle stack described above. By integrating the power density of Joule losses in a single layer ($\int_{V_i} p_J \mathrm{d}V_i = \int_{V_i} \sigma_i |E_i|^2 \mathrm{d}V_i$) and dividing by the total dissipated power, the weighting factor for the muscle and skin is, in this case, found to be 68% and 28%, respectively.

IV. MMIC Dicke Radiometer Design

In this section, the design of the GaAs MMIC, which includes a single-pole double-throw (SPDT) switch and three-stage LNA, is described. Both switch and LNA are implemented in the 110-nm PIH1-10 WIN Semiconductors GaAs process and are characterized first separately and then integrated into a single die.

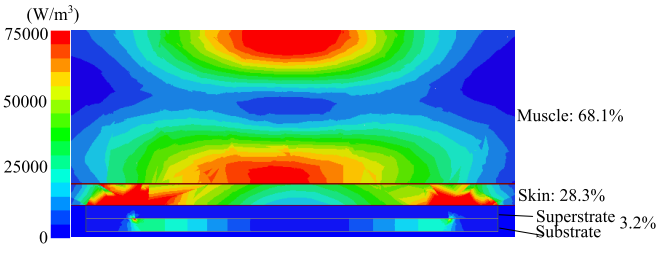

Fig. 6. Full-wave simulations of volume Joule loss density (W/m^3) of the near-field antenna on a skin–muscle phantom with 1 W at the feed. The weighting factors (percentages of total power) are also stated, with 3% of the total power being in the surrounding air and unaccounted for here.

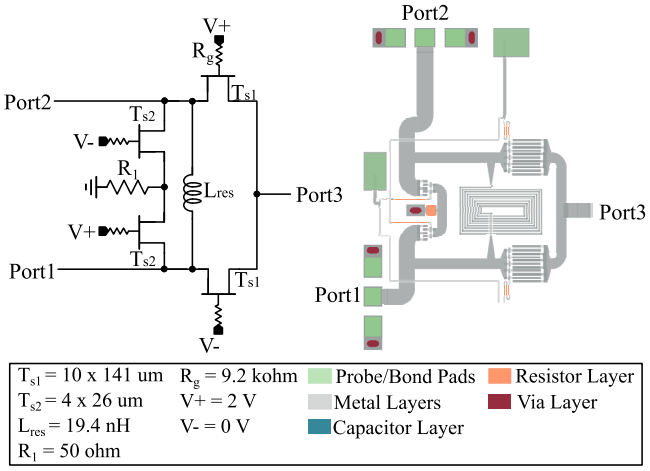

Fig. 7. Circuit schematic (left) and layout (right) of the SPDT switch. Parameter values and the main metal, via, pad, capacitor, and resistor layers are shown. Several process layers are removed for clarity.

A. SPDT Switch Design and Measurement

Fig. 7 shows the circuit schematic, layout, and parameter values of an absorptive SPDT switch chosen for this design. The switch insertion loss is important because it is the first component of the radiometer and directly contributes to noise. The isolation should be better than 30 dB so that a noise power corresponding to less than 0.3 K from the reference load leaks into the near-field antenna port. The return loss should be higher than 10 dB for an SNR reduction of less than 10% for power transfer to the LNA. The SPDT switch uses a shunt-series topology for high isolation. The transistors are turned on and off by biasing the gate to 2 and 0 V, respectively. R_1 is a 50-Ω resistor seen at the OFF port when T_{s2} is on. This reduces the reflection coming in from the OFF port. The inductor between the shunt and series transistors is used to create a resonance with the parasitic capacitance of the OFF transistors, improving the insertion loss and isolation of the switch. The OFF capacitors of T_{s1} and T_{s2} are 0.7 and 0.06 pF, respectively. An inductor L_{res} is used to create resonance with these two capacitors. The resonating inductor also biases all the nodes in the switch, avoiding extra loss and

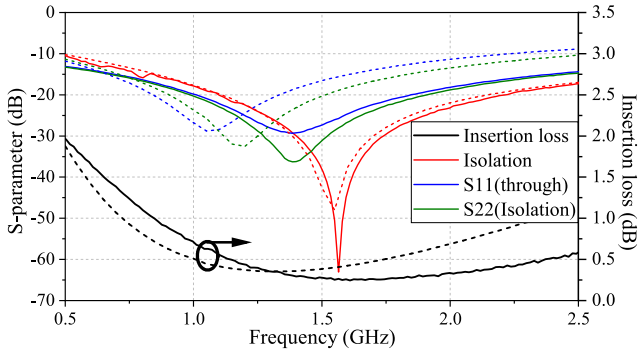

Fig. 8. Measured (solid line) and simulated (dashed line) performance of the MMIC SPDT switch.

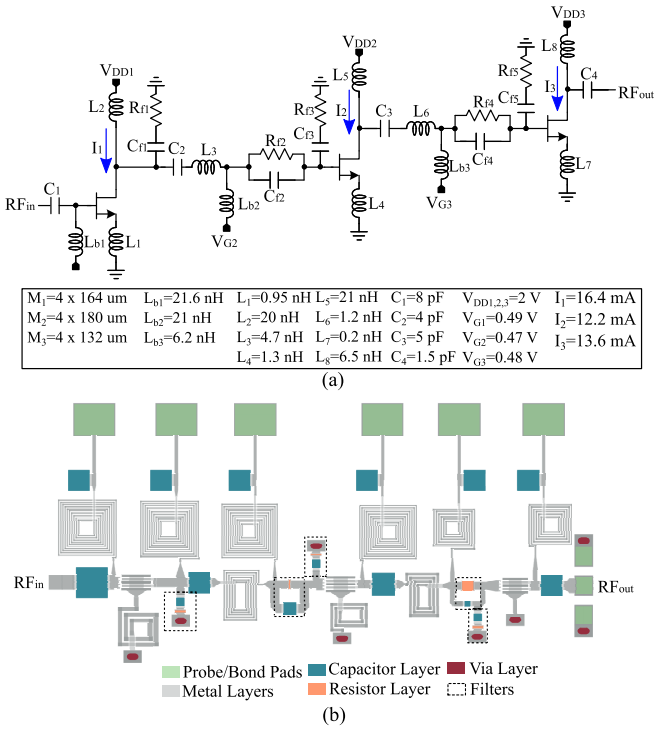

Fig. 9. (a) Circuit schematic and component values for the three-stage LNA integrated into a GaAs MMIC. The element values and bias points are shown in the table. Five distributed filters are used as matching and stability networks. (b) Layout of the chip, where the used layers are shown with different colors.

voltage drop from biasing resistors. Fig. 8 shows the measured and simulated switch performance. The minimum insertion loss is 0.24 dB at 1.61 GHz, and the maximum isolation is 63 dB at 1.58 GHz. At the design frequency of 1.4 GHz, the insertion loss is 0.29 dB and the isolation is 30.8 dB. A slight frequency shift is shown for the return loss due to an impedance mismatch of the load termination during the measurement. The dimensions of the switch are 0.9 × 0.9 mm.

B. LNA Design

Since >45 dB of gain is required at 1.4 GHz and a low-noise figure, a three-stage LNA is designed [27]. Fig. 9(a) shows the circuit schematic, circuit component values, and bias points of the LNA. The stability of an LNA is crucial since the LNA is multistage with >45-dB gain. Several techniques improve the stability, including the use of a source degeneration inductor

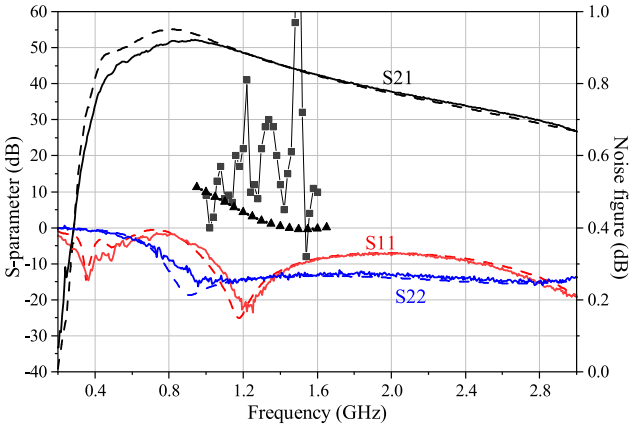

Fig. 10. Measured (solid line) and simulated (dashed line) S-parameter magnitudes of the LNA MMIC. The reverse isolation $|S_{12}|$ is below the noise floor of the measurement setup. The measured noise figure is shown with square symbols, while the simulation is shown with triangle symbols.

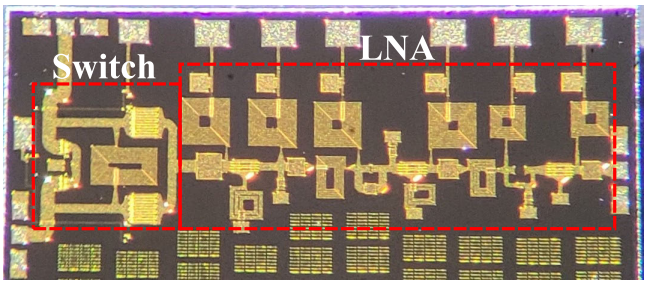

Fig. 11. Photograph of the GaAs MMIC SPDT switch and a three-stage LNA. The total chip dimensions are 3.75 × 1.7 mm.

as a feedback technique [28] and the use of an RC shunt filter at the output to avoid negative resistance [29]. The LNA design achieves stability using source degeneration and five RC filters that operate as an interstage matching network. For multiple-stage LNAs, multiple filters are needed to ensure stability in all stages. The distribution of the filters allows improved stability with less than 0.02-dB noise figure degradation according to simulation.

The layout of the LNA with dimensions 2.6 × 1 mm is shown in Fig. 9(b), where the device sizes and biasing are also given. The LNA power consumption is 84.4 mW. Fig. 10 shows the measured and simulated S-parameter magnitudes. The peak gain is 52.3 dB at 0.94 GHz and the gain at 1.4 GHz is 45.2 dB, which satisfies the aforementioned gain requirement. The measured $|S_{11}| < -10$ dB is for 1.05–1.5 and 2.45–3.7 GHz and the measured $|S_{22}| < -10$ dB is for 0.83–3.3 GHz. The noise figure was measured using a Keysight 8970B noise figure meter with a 346B noise source, and at 1.4 GHz, $\mathrm{NF_{LNA}} = 0.52$ dB.

V. Radiometer Implementation

Both the SPDT switch and LNA are implemented on a single GaAs MMIC with a die size of 3.75 × 1.7 mm, as shown in Fig. 11. For characterization, the MMIC is packaged on a 45 × 45 mm printed circuit board (PCB) of 0.254-mm-thick Rogers 4350B substrate. Fig. 12 shows the S-parameter measurements of the packaged LNA together with

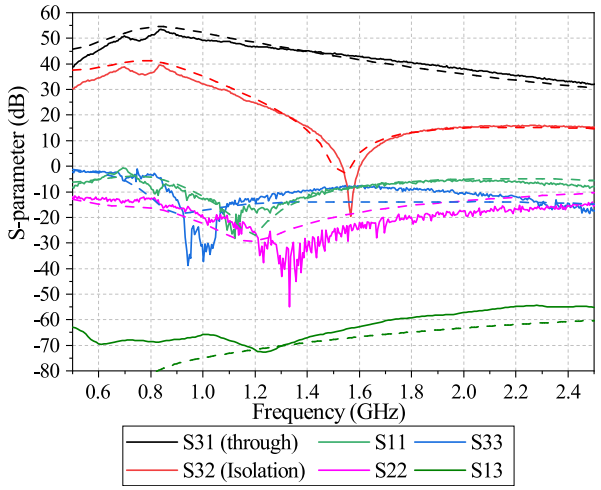

Fig. 12. Measured (solid line) and simulated (dashed line) S-parameter magnitudes of the packaged SPDT switch and LNA MMIC portion of the Dicke radiometer. A coaxial calibration is performed on the connector reference planes.

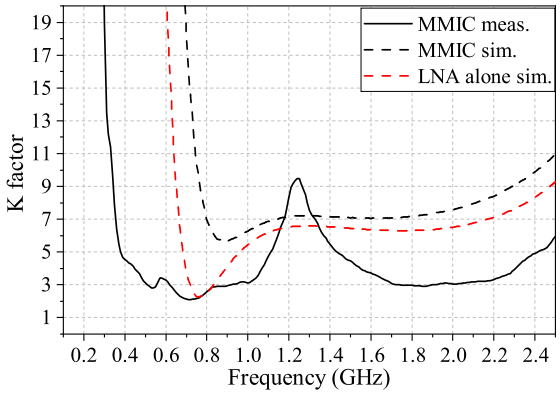

Fig. 13. Measured and simulated stability K factor of the MMIC (LNA with switch) as well as simulated LNA K factor. The measured K factor of the LNA alone is not calculated since the reverse isolation was below the noise floor in the S-parameter measurement.

the SPDT switch. The gain of the through ports (from ON switch input to LNA output) at 1.4 GHz is 45.1 dB, and the gain through the isolation port (from OFF switch input to LNA output) is 15.5 dB. The return loss at 1.4 GHz is above 10 dB at all ports. The resonance at 0.8 GHz is due to the biasing structure involving a 0.2-nH inductor and a 100-pF shunt capacitor. To verify stability, the measured and simulated K factor is shown in Fig. 13. The measured and simulated noise figure of the through port is shown in Fig. 14, and at 1.4 GHz, $NF_{rad} = 0.88$ dB.

To limit received noise power bandwidth and reduce out-of-band interference, two off-chip bandpass filters are connected to the output of the packaged MMIC (see Fig. 3). The first bandpass filter [30] has a bandwidth of 160 MHz from 1.32 to 1.48 GHz and an out-of-band rejection of 32–41 dB from dc to 2.4 GHz. The second bandpass filter is an surface acoustic wave (SAW) filter that has a narrower bandwidth of 64 MHz from 1.38 to 1.44 GHz [31]. Including the filter loss, the gain at 1.4 GHz is 41.9 dB and the gain across frequency near the operating band is shown in Fig. 15. The 3-dB bandwidth of

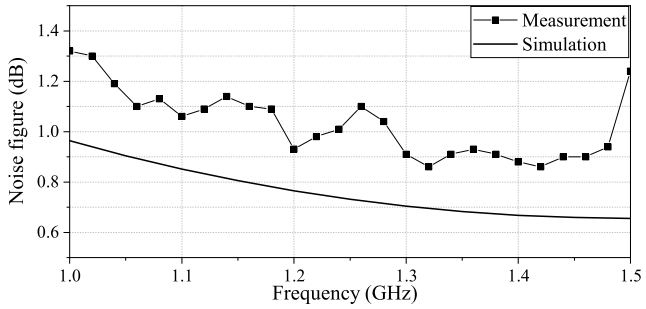

Fig. 14. Measured and simulated noise figure of the packaged SPDT switch and LNA MMIC front end of the Dicke radiometer.

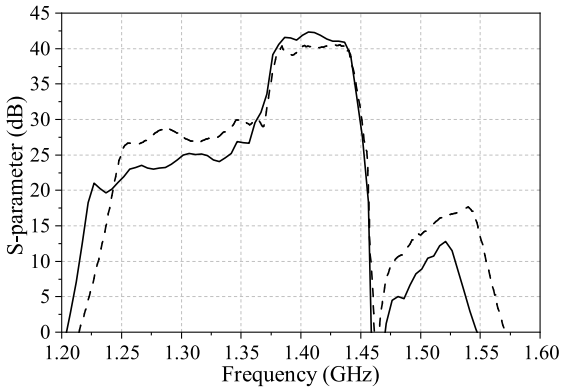

Fig. 15. Measured (solid line) and simulated (dashed line) gain from the input of the ON switch of the packaged MMIC to the output of the off-the-shelf bandpass filters. The gain has a 3-dB bandwidth of 64 MHz from 1.38 to 1.44 GHz.

the radiometer is about 63 MHz from 1.377 to 1.44 GH, wider than the targeted 27-MHz bandwidth.

Since the integration time [τ in (2)] can be long for thermal measurement time scales, we attempt bandwidth reduction to minimize interference. Narrowband matching of the detector is used to reduce the radiometer bandwidth from 62 to 60 MHz. The detector is designed with the Skyworks SMS7630-079 diode, integrated with a matching circuit comprising a $\lambda/4$ resonator and shunt capacitors. This configuration effectively matches the impedance characteristics of the diode over a frequency range of approximately 60 MHz centered around 1.412 GHz [32]. The rectified dc voltage is amplified through a postdetection amplification stage, featuring a voltage gain of 100 V/V. This amplification is integrated into the identical board of the detector. The dc amplifier operates within a 5-V voltage range while consuming a current of under 1 mA.

Fig. 16 shows the responsivity of the radiometer from the input through port to the output of the dc postamplification stage. The measurement is done with a sinusoidal signal at 1.4 GHz at the input to the radiometer. The voltage responsivity of the full radiometer at 1.4 GHz is 213 GV/W, assuming a 1-MΩ dc load and a 50-Ω input impedance. The measured voltage responsivity at the output of the detector for an RF input signal at the switch port when the switch is on is shown in Fig. 17 and is a function of frequency over the operating bandwidth.

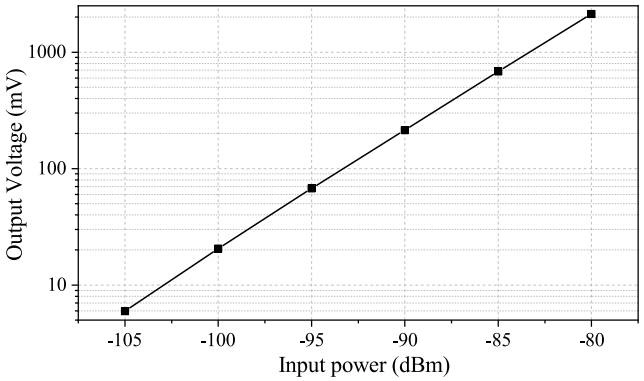

Fig. 16. Measured voltage responsivity of the radiometer from the through port to the output of the dc amplifier. The responsivity is 213 GV/W at 1.4 GHz.

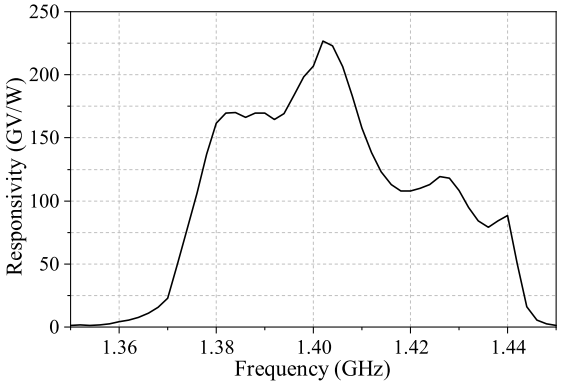

Fig. 17. Measured frequency response of the entire Dicke radiometer responsivity when the input switch is on.

The gain impacts the sensitivity due to the oscilloscope resolution limit. The voltage amplitude resolution of the oscilloscope (DSOX1102G) is 3.14 μV, and the corresponding $\Delta T = \Delta V/(kBR(f)) = 0.0226$ K, where k is Boltzmann's constant, $B = 100$ MHz is the measurement bandwidth, and $R(f)$ is the frequency-dependent full receiver detector voltage responsivity in V/W. This calculation does not consider any input noise, and therefore, the uncertainty from the oscilloscope resolution is 0.0226 K and this reduces the sensitivity of the radiometer. The impact of the LNA and switch noise figure on radiometer sensitivity can be estimated based on the measured noise figure, gain, and detector responsivity. The 0.88-dB noise figure of the front end translates to a noise temperature $T_A = 65.1$ K. The corresponding increase in detected voltage due to this noise is found by integrating the responsivity of the radiometer (including the detector and filter) across the operating bandwidth from 1.35 to 1.45 GHz. This results in $\Delta V = kT_ABR = 9$ mV. The Allan deviation of the output voltage of the radiometer is shown in Fig. 18 for integration times from 10 μs to 100 s.

VI. Temperature Measurements

Temperature measurements are done with the radiometer input connected to the near-field antenna placed directly on the skin tissue phantom. A bag of saline muscle phantom is placed under the skin phantom and is either hot (at 60 °C)

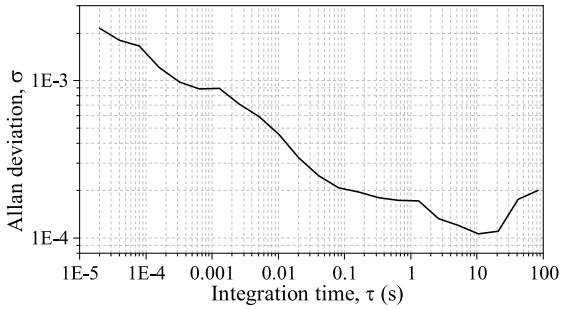

Fig. 18. Allan deviation of the Dicke radiometer to 100-s integration time, obtained from measured data. A minimum in the Allan deviation is observed at an integration time of approximately 10 s, with a value on the order of 1.06×10^{-4}. In this work, an integration time of $\tau = 2$ s is used, with a corresponding Allan deviation of 1.7×10^{-4}.

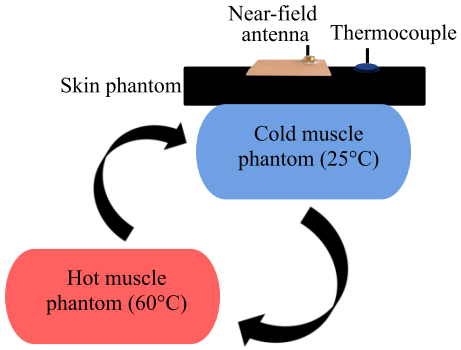

Fig. 19. Illustration of the two-layer measurement setup. Two bags of saline muscle phantom are used. One is a hot phantom at 60 °C, and the other is a cold phantom kept at room temperature, 25 °C. These two phantoms are placed alternately one at a time under the skin phantom. The output voltage is then data processed and the estimated temperature is compared to the real "ground truth" temperature.

TABLE II
Electrical Properties of Materials at 1.4 GHz [25], [26]

Material	Thickness (mm)	ϵ_r	σ(S/m)
Skin phantom	2	28	0.84
Saline	15	77.7	1.26
Playdoh	15	32	5.4
Skin (cheek)	2	39.6	1.04
Fat (cheek)	2	5.4	0.06
Muscle (cheek)	2	54.1	1.14

or cold kept at room temperature (25 °C). In the experiment, two saline bags are alternated, as shown in Fig. 19. Since the temperature of the muscle can be controlled in this experiment, the calculated weighting factors $W_{1,2}$ can be validated. Table II gives permittivities and conductivities of the materials used in the experiments in this section.

For these measurements, the radiometer is calibrated against a reference noise source, and in this case, a matched 50-Ω coaxial load held at 25 °C controlled by a ThorLabs MTD415T thermistor temperature controller. The load is placed on top of a Peltier element connected to a heat sink. The load is thermally isolated using polystyrene foam. The output dc

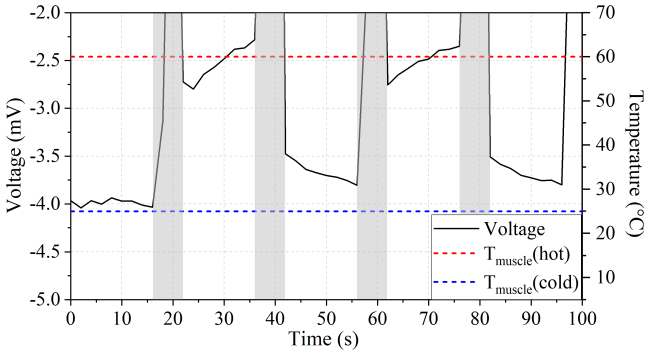

Fig. 20. Measured calibrated output of the detector when a hot (60 °C) and cold (25 °C) muscle phantom is placed under the skin phantom approximately at 20-s intervals. The output voltage increases with the hot muscle phantom, as expected. The spikes around 20, 40 s, and so on, shaded in gray, are periods when the muscle phantom is alternated and the antenna is thus not behaving as designed.

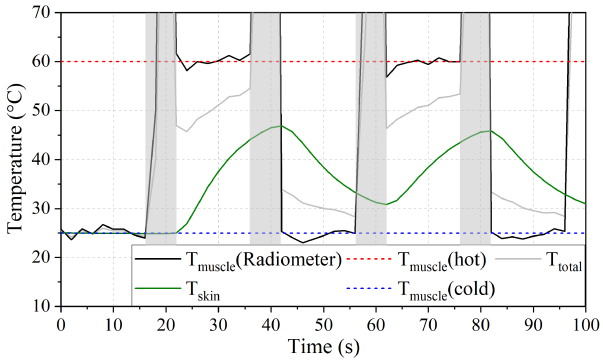

Fig. 21. Measured temperature of the muscle tissue phantom, using T_{skin} (green line) measured by a thermocouple and subtracted in the algorithm. The red and blue dotted lines show the temperatures of the water bath used to set the known phantom temperature, 60 °C and 25 °C.

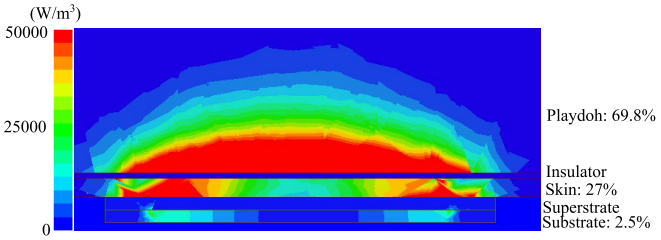

Fig. 22. Full-wave simulations of volume Joule loss density (W/m^3) with 1 W at the feed. Playdoh is used as a muscle phantom instead of saline, as shown in Fig. 6. A thermal insulator is placed between the skin and muscle layer to delay the time of thermal equilibrium. The weighting factors (percentages of total power) are also stated.

voltage of the radiometer, captured on a sampling oscilloscope, measures both the signal from the near-field antenna and the signal from the reference noise source. The calibration is done in the data processor by subtracting the two voltages. This calibration reduces the effects of gain fluctuation of the components.

Fig. 20 shows the measured and calibrated output dc voltage of the radiometer. At the start of the measurement ($t = 0$), the cold muscle phantom is in place. After about 20 s, the cold muscle phantom is replaced by the hot phantom. During this transient of about 5 s, the near-field antenna is not operating as designed, and thus, the voltage in these intervals is not meaningful and is shaded in gray in the plot. With the cold muscle phantom, the radiometer shows lower voltage than with the heated muscle phantom, as expected.

A temperature retrieval algorithm is used to estimate the temperature of the muscle layer. The radiometer measures the total noise temperature from the skin and muscle phantoms in addition to the ambient temperature. Assuming that the ambient contribution is negligible, the total radiometric temperature can be written as a weighted sum

$$T_{\text{total}} = W_{\text{skin}} T_{\text{skin}} + W_{\text{muscle}} T_{\text{muscle}} \tag{4}$$

where the coefficients W_{skin} and W_{muscle} are found from the percentage of noise power in each of the two separate layers, calculated by integration of the simulated volume loss power density using reciprocity [15]. The assumption of negligible ambient contribution is validated in simulations, which result in an environment weighting factor below 5%. Fig. 6 shows the simulated volume Joule loss density of the near-field antenna and phantom tissue stack simulated in transmission with 1 W of input power at the probe feed. The coefficients are found as the ratio of the Joule loss in a particular volume to the total Joule loss in the whole stack up, and the values are shown in Fig. 6. The tissue stack volume in the simulations is truncated to 6 × 6 × 1.7 cm, and a larger size derives the same results. The temperature of the skin phantom, T_{skin} is independently measured by an individual thermocouple in direct contact with the skin and assumed to be known. The temperature of the muscle, T_{muscle}, is calculated from (4). Fig. 21 shows T_{muscle} compared to the actual known temperature of the saline phantom. The average error is 0.77 °C and the maximum error is 3.2 °C.

A. Measurements With a Different Muscle Phantom

A second temperature measurement is done using playdoh as a muscle phantom instead of a saline bag, with properties given in Table II. The measurement using a saline plastic bag has the limitation of unavoidable air bubbles, which occur in different parts of the phantom during different time intervals of the measurement. An additional limitation is that the actual temperature of the muscle phantom is known for a limited time after the saline phantom is taken out from a heated water bath, which affects measurement accuracy. In contrast, the true-time temperature of the playdoh phantom can be sampled with a thermocouple placed inside the playdoh. For this temperature test, a thermal insulator is placed between the skin and muscle phantoms to slow down the time to reach thermal equilibrium, allowing the temperatures of the muscle and skin to be different for a longer period. Due to the electrical property differences between the playdoh and the saline phantoms, shown in Table II, the weighting factors are also different, as shown in Fig. 22.

The temperature measurement takes 400 samples over about 45 min. The test uses hot and cold muscle phantoms, and both measurement results are shown in Fig. 23. The test with the hot

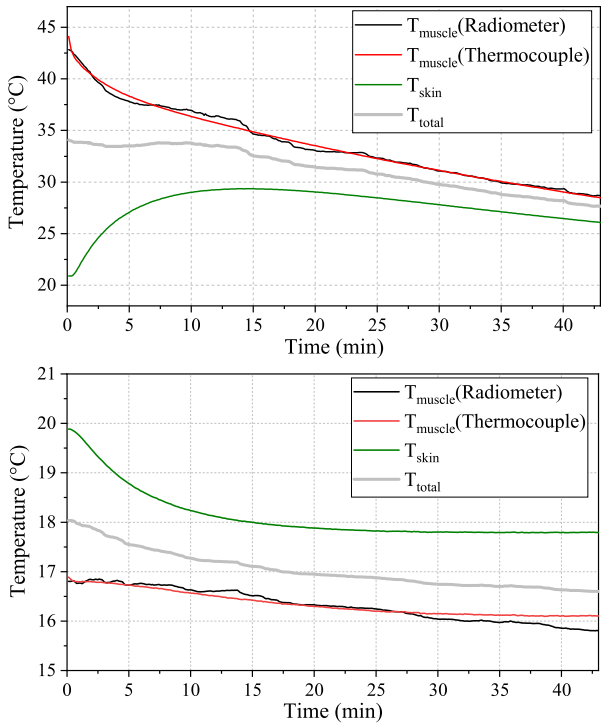

Fig. 23. Temperature measurement (with thermocouple) and estimation (from radiometer output) when playdoh muscle phantom is placed under the skin phantom. Both hot playdoh (top) and cold playdoh (bottom) tests are conducted for validation across temperatures.

muscle phantom shows that it cools as the skin phantom heats. The skin phantom temperature is subtracted from the total temperature, using the same method as for the saline phantom. However, the algorithm uses a different weighting factor value (27% for skin instead of 28.3%). The estimated muscle phantom temperature matches the real-time value measured with a thermocouple with an average error of 0.247 °C and a maximum error of 1.25 °C. The thermocouple is placed at the bottom of the playdoh about 3 mm above the insulator since this is the area where most of the blackbody radiation originates due to the high Joule loss.

A second test is done with a cooled playdoh phantom. The estimation, in this case, has an average error of 0.1 °C and a maximum error of 0.31 °C compared to the actual measured temperature. This test verifies that the radiometer can measure buried layer temperatures both above and below room temperature.

B. Noninvasive Passive In Vivo Temperature Measurements

In vivo measurements are done using temperature-varying tap water inside the mouth. This measurement is passive and noninvasive, with water temperature that can be varied in the mouth, and the near-field antenna placed on the cheek, as shown in the photograph in Fig. 24. The same near-field antenna used in previous tests with phantoms is reasonably well-matched to tissue layers of the human cheek

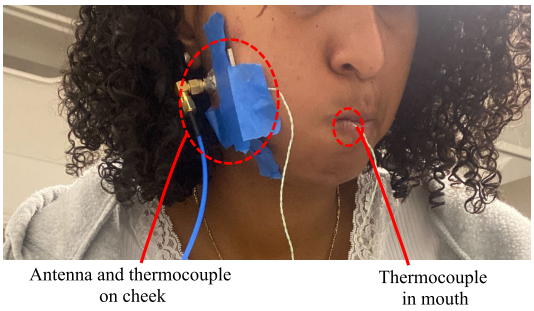

Fig. 24. In vivo measurement conducted on a human cheek. The near-field antenna is placed on the cheek to measure the temperature of hot or cold water inside the mouth. A thermocouple is placed inside the mouth to independently measure water temperature. (Courtesy: Sofia Mvokany, University of Colorado at Boulder.)

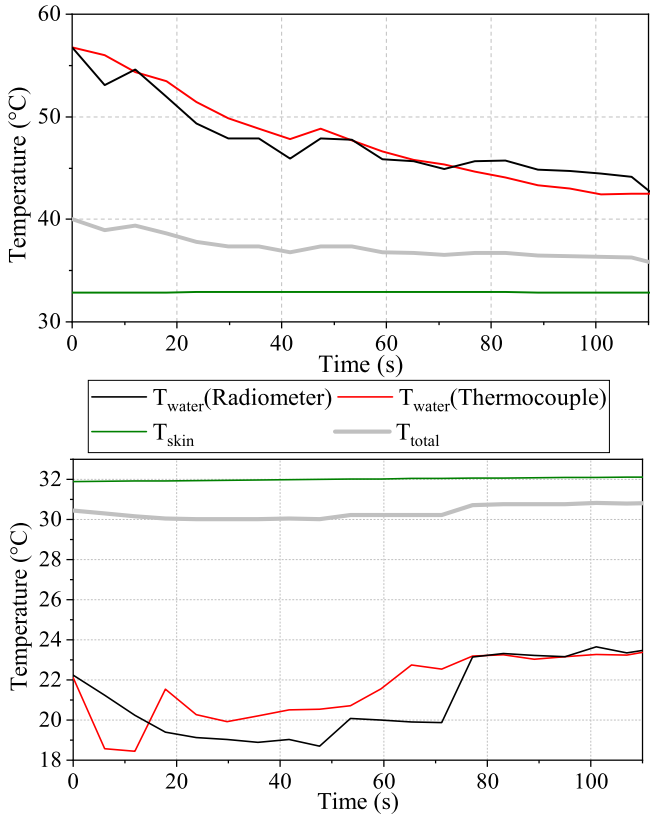

Fig. 25. In vivo temperature measurements on the cheek with hot water (top) and cold water (bottom) in the mouth. The temperature of the skin and the water inside the mouth is measured independently with thermocouples.

with properties given in [33]. In this test, a circulator is connected between the antenna and the input of the radiometer to avoid power fluctuations due to antenna mismatch. With the near-field antenna attached on the cheek, a thermocouple is placed inside the mouth to measure the actual temperature of the water. Another thermocouple is placed on the skin next to the antenna to monitor any temperature change of the skin. Hot and cold water is held in the mouth for 20 samples (about 110 s) as the radiometer measures the temperature change of the water. The temperature of the skin did not change during these measurements.

TABLE III
WEIGHTING FACTORS OF TISSUE LAYERS WITH SKIN PROPERTY VARIATION

Property	Mean value	STD dev	Max W_{skin}	Min W_{skin}
Thickness	2 mm	8%	0.291	0.265
ϵ_r	28	10%	0.303	0.259
σ	0.84 S/m	10%	0.298	0.261

Equation (3) is used to estimate the water inside the cheek, using weighting factors calculated by full-wave simulations of the near-field antenna placed on the cheek tissue stack of skin, fat, and muscle with properties shown in Table II. The calculated weighting factor of the water inside the cheek is $W_{\text{water}} = 17\%$, and the estimated temperature results of these measurements are shown in Fig. 25. The radiometer estimation follows the real-time thermocouple temperature measurement of the water with an average error of 1.17 °C.

VII. CONCLUSION AND DISCUSSION

In summary, this article demonstrates a switch and stable 45-dB gain LNA implemented on a GaAs MMIC with a noise figure of 0.88 dB at 1.4 GHz, showing for the first time that a radiometer for internal body temperature can be miniaturized by MMIC integration. With a near-field antenna probe at the input to the MMIC, discrete filters, and a detector stage at the output, 60-MHz bandwidth measurements are obtained on a skin–muscle phantom to track the muscle temperature. Properties of tissue layers, however, including thickness, permittivity, and conductivity, vary from person to person and from one part of the body to another. Thus, we investigated in simulations the effect of this variation on the measured temperature of a subcutaneous tissue layer.

A. Temperature Estimation Sensitivity

The sensitivity of the temperature estimate depends on the values of the weighting factors that, in turn, depend on tissue property variations. For example, the relative permittivity of dry and wet skin can vary by ±6% at 1.4 GHz [26], while forehead skin thickness can vary by ±8% between different human bodies [34]. This literature provides standard deviation values for the properties of human skin, which we use to determine the property range in the simulation. The weight of the skin changes by 2.6 percentage points (pp) when the thickness is varied from 1.84 to 2.16 mm. When varying the permittivity and conductivity, the weight of the skin changes by 4.4 and 3.7 pp, respectively. For the simulations we considered, the permittivity of the skin had the largest impact on the weighting factor values. More details about the tolerance are shown in Table III.

Fig. 26 shows the volume Joule loss density for two skin layer property scenarios, Cases 1 and 2, where all three properties are varied to extreme conditions. The muscle phantom thickness is constant for all simulations as it matches the dimensions used in measurement setups. In Case 1, the weight of the skin is at its lowest. The skin has thickness, permittivity, and conductivity of $h = 1.84$ mm, $\epsilon = 30.8$, and $\sigma = 0.756$ S/m, respectively. Due to the reduced loss of the skin layer, the excitation from the near-field antenna senses deeper into the muscle, increasing the weight of the muscle. The weights corresponding to this configuration are $W_{\text{skin}} = 0.227$ and $W_{\text{muscle}} = 0.739$. The weighting factor of the muscle increased by 5.8 pp compared to the simulation done without the variation, as shown in Fig. 6.

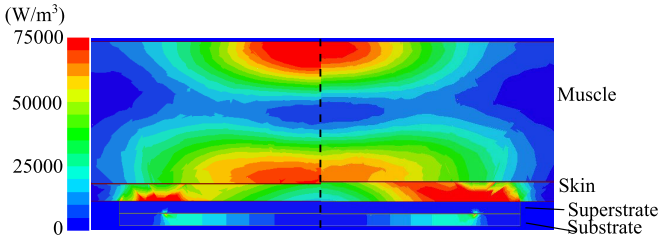

Fig. 26. Side-by-side comparison of simulated volume loss density when skin properties are varied. Left: skin phantom properties: thickness, $h = 1.84$ mm, $\epsilon = 30.8$, and $\sigma = 0.756$ S/m. The resulting skin weighting factor is 22.7%. Right: skin phantom properties: $h = 2.16$ mm, $\epsilon = 25.2$, and $\sigma = 0.924$ S/m. The resulting skin weighting factor is 33.5%.

Case 2, when the weight of the skin is at its highest, has thickness, permittivity, and conductivity of $h = 2.16$ mm, $\epsilon = 25.2$, and $\sigma = 0.924$ S/m, respectively. The weighting factors of the phantom layers are $W_{\text{skin}} = 0.335$ and $W_{\text{muscle}} = 0.634$. In contrast to Case 1, the weighting factor of the muscle decreased by 4.7 pp compared to the simulation done without the variation. Thus, the variation in muscle weighting factor may vary up to 10.5 pp, given nominal physiological skin tissue properties. In both cases, the simulated reflection coefficient and radiated power have negligible differences of less than 0.4%.

Using the radiometer output voltage data shown in Fig. 20, different skin layer weighting factor values result in different muscle temperature estimation errors. For Case 1, where the skin weight is lowest, the average error increases to 1.14 °C with a maximum error of 4.04 °C. Meanwhile, for Case 2, the average error increases to 1.58 °C with a maximum error of 4.62 °C. This is a 0.37 °C and 0.81 °C increase from the original average error of 0.77 °C. Knowledge of the tissue properties reduces the estimation error by improving the computation of the layer weights. Average temperature estimation errors are <2 °C, even without consideration of the tissue properties. Thus, the absolute error in temperature estimation for real medical use cases, in which the temperature swing would be roughly 5 °C [35], is expected to be smaller.

B. Conclusion

In conclusion, this article demonstrates that a Dicke radiometer with GaAs MMIC front-end switch and LNA can be used with a near-field antenna to measure the temperature of a buried tissue layer. The near-field antenna is designed to receive blackbody radiation from a 15-mm-thick muscle

phantom under a 2-mm-thick skin phantom. This configuration was assembled and tested, with a difference in radiometric temperature measurements of the subcutaneous muscle layer, compared to a thermocouple "ground truth" measurement, averaging 0.77 °C. Several other tests were performed, including measurements with a different muscle phantom as well as a noninvasive, passive in vivo measurement of water inside the human cheek. These measurements illustrate similar agreement between radiometric and direct-contact temperature measurements. An additional consideration necessary for the clinical application of microwave thermometry is the impact of tissue property variation on the accuracy of internal layer temperature estimation, which is investigated here in simulations and shows that up to 10.5 pp of skin weight factor can change. Finally, the power consumption of this radiometer is about 80 mW, compared to >0.5 W for a similar device with off-the-shelf components.

ACKNOWLEDGMENT

The authors thank WIN Semiconductors and Dr. D. Danzilio for circuit fabrication as a part of a graduate course at the University of Colorado at Boulder, Boulder, CO, USA. They thank Sofia Mvokany at the University of Colorado for help during the in vivo measurements. Dielectric properties of playdoh were provided by Dr. Milica Popović, McGill University, Montreal, QC, Canada.

REFERENCES

[1] F. Biancari, T. Juvonen, and G. Speziale, "Commentary: Cooling the brain for elective aortic hemiarch repair," *J. Thoracic Cardiovascular Surg.*, vol. 165, no. 5, pp. 1774–1775, May 2023.

[2] C. L. Lim, C. Byrne, and J. K. Lee, "Human thermoregulation and measurement of body temperature in exercise and clinical settings," *Ann. Acad. Med., Singap.*, vol. 37, no. 4, pp. 347–353, Apr. 2008.

[3] A. S. Howe and B. P. Boden, "Heat-related illness in athletes," *Amer. J. Sports Med.*, vol. 35, no. 8, pp. 1384–1395, Aug. 2007.

[4] L. C. Lack, M. Gradisar, E. J. W. Van Someren, H. R. Wright, and K. Lushington, "The relationship between insomnia and body temperatures," *Sleep Med. Rev.*, vol. 12, no. 4, pp. 307–317, Aug. 2008.

[5] V. M. Ravi, A. K. Sharma, and K. Arunachalam, "Pre-clinical testing of microwave radiometer and a pilot study on the screening inflammation of knee joints," *Bioelectromagnetics*, vol. 40, no. 6, pp. 402–411, Sep. 2019.

[6] A. Y. Owda, N. Salmon, S. Shylo, and M. Owda, "Assessment of bandaged burn wounds using porcine skin and millimetric radiometry," *Sensors*, vol. 19, no. 13, p. 2950, Jul. 2019.

[7] P. Wust et al., "Hyperthermia in combined treatment of cancer," *Lancet. Oncol.*, vol. 3, no. 8, pp. 487–497, 2002.

[8] G. Galiana, R. T. Branca, E. R. Jenista, and W. S. Warren, "Accurate temperature imaging based on intermolecular coherences in magnetic resonance," *Science*, vol. 322, no. 5900, pp. 421–424, Oct. 2008.

[9] S. Mendt et al., "Circadian rhythms in bed rest: Monitoring core body temperature via heat-flux approach is superior to skin surface temperature," *Chronobiol. Int.*, vol. 34, no. 5, pp. 666–676, May 2017, doi: 10.1080/07420528.2016.1224241.

[10] CORE. *The Core Sensor Technology*. Accessed: Jul. 1, 2023. [Online]. Available: https://corebodytemp.com/pages/the-core-body-temperature-sensor-technology

[11] Maya0851601054. (Jul. 2021). *3D Rendering Illustration of Lymphatic System Stock Illustration*. [Online]. Available: https://www.dreamstime.com/d-rendering-illustration-lymphatic-system-orange-lymphatic-system-front-view-image225146687

[12] B. Enander and G. Larson, "Microwave radiometric measurements of the temperature inside a body," *Electron. Lett.*, vol. 10, no. 15, p. 317, 1974.

[13] J. Edrich and P. C. Hardee, "Thermography at millimeter wavelengths," *Proc. IEEE*, vol. 62, no. 10, pp. 1391–1392, Oct. 1974.

[14] S. Mizushina, H. Oh-ishi, and Y. Hamamura, "A three-band microwave radiometer for noninvasive temperature measurement," in *IEEE MTT-S Int. Microw. Symp. Dig.*, 1984, pp. 145–146.

[15] P. Momenroodaki, W. Haines, M. Fromandi, and Z. Popovic, "Noninvasive internal body temperature tracking with near-field microwave radiometry," *IEEE Trans. Microw. Theory Techn.*, vol. 66, no. 5, pp. 2535–2545, May 2018.

[16] S. G. Vesnin et al., "Portable microwave radiometer for wearable devices," *Sens. Actuators A, Phys.*, vol. 318, Feb. 2021, Art. no. 112506.

[17] J. Lee, G. S. Botello, R. Streeter, and Z. Popovic, "Noninvasive internal body thermometry with on-chip GaAs Dicke radiometer," *IEEE Microw. Wireless Technol. Lett.*, vol. 33, no. 6, pp. 1–4, Apr. 2023.

[18] F. T. Ulaby et al., *Microwave Radar and Radiometric Remote Sensing*, vol. 4, no. 5. Ann Arbor, MI, USA: Univ. Michigan Press, 2014.

[19] A. R. Kerr, "On the noise properties of balanced amplifiers," *IEEE Microw. Guided Wave Lett.*, vol. 8, no. 11, pp. 390–392, Nov. 1998.

[20] J. Lee, G. S. Botello, R. Streeter, K. Hall, and Z. Popovic, "A hybrid correlation-Dicke radiometer for internal body thermometry," in *Proc. 52nd Eur. Microw. Conf. (EuMC)*, Sep. 2022, pp. 464–467.

[21] E. Villa, N. Arteaga-Marrero, G. León, L. F. Herrán, I. Mateos, and J. Ruiz-Alzola, "A 3.5-GHz pseudo-correlation type radiometer for biomedical applications," *AEU-Int. J. Electron. Commun.*, vol. 130, Feb. 2021, Art. no. 153558. [Online]. Available: https://www.sciencedirect.com/science/article/pii/S143484112032762X

[22] I. Kim et al., "Dual-band on-body near field antenna for measuring deep core temperature with a microwave radiometer," *IEEE Access*, vol. 10, pp. 63715–63722, 2022.

[23] M. K. Sedankin, I. V. Nelin, V. Yu. Leushin, V. A. Skuratov, L. Y. Mershin, and S. G. Vesnin, "System of rational parameters of antennas for designing a multi-channel multi-frequency medical radiometer," in *Proc. Int. Conf. Actual Problems Electron Devices Eng. (APEDE)*, Sep. 2020, pp. 154–159.

[24] K. L. Hall, R. Streeter, and Z. Popovic, "Near-field antenna for noninvasive human head microwave thermometry," in *Proc. IEEE Int. Symp. Antennas Propag. USNC-URSI Radio Sci. Meeting (AP-S/URSI)*, Jul. 2022, pp. 880–881.

[25] Spaeg. *Customized Generic Phantoms*. Accessed: Dec. 1, 2022. [Online]. Available: https://speag.swiss/components/phantoms/customized-2/customized-generic-phantoms-2/

[26] D. Andreuccetti. (2012). *An Internet Resource for the Calculation of the Dielectric Properties of Body Tissues in the Frequency Range 10 Hz-100 GHz*. [Online]. Available: http://niremf.ifac.cnr.it/tissprop/

[27] J. Lee and Z. Popovic, "A GaAs LNA MMIC for a correlation-Dicke radiometer internal-body temperature sensor," in *Proc. IEEE Radio Wireless Symp. (RWS)*, Jan. 2023, pp. 31–33.

[28] S. Wang, "A GaAs MMIC LNA design for wideband satellite communication receiver application," in *Proc. IEEE Int. Conf. Communiction Problem-Solving*, Dec. 2014, pp. 631–633.

[29] A. M. Bassal and A. H. Jarndal, "GaN low noise amplifier design for Wimax applications," in *Proc. 16th Medit. Microw. Symp. (MMS)*, Nov. 2016, pp. 1–4.

[30] Mini-Circuits. *Cbp-1400e+ Ceramic Resonator Band Pass Filter*. Accessed: Jun. 1, 2023. [Online]. Available: https://www.minicircuits.com/WebStore/dashboard.html?model=CBP-1400E%2B

[31] TAI-SAW. *Saw Filter 1412 MHZ SMD*. Accessed: Jun. 1, 2023. [Online]. Available: https://www.taisaw.com/upload/product/TA2313A%20_Rev.1.0_.pdf

[32] R. Streeter, G. S. Botello, K. Hall, and Z. Popovic, "Correlation radiometry for subcutaneous temperature measurements," *IEEE J. Electromagn., RF Microw. Med. Biol.*, vol. 6, no. 2, pp. 230–237, Jun. 2022.

[33] C. Gabriel, "Compilation of the dielectric properties of body tissues at RF and microwave frequencies," Dept. Phys., King's Coll London, U.K., Tech. Rep. N.AL/OE-TR-1996-0037, 1996.

[34] K. Tisdale, A. Bringer, and A. Kiourti, "Development of a coherent model for radiometric core body temperature sensing," *IEEE J. Electromagn., RF Microw. Med. Biol.*, vol. 6, no. 3, pp. 355–363, Sep. 2022.

[35] J. E. Hall and M. E. Hall, "Body temperature regulation and fever," in *Guyton and Hall Textbook of Medical Physiology*, 14th ed. Sait Louis, MO, USA: Elsevier, 2021, ch. 74, pp. 901–902.

Jooeun Lee (Graduate Student Member, IEEE) received the B.S. degree in electronics engineering from Pusan National University, Busan, South Korea, in 2019, and the M.S. degree in electrical engineering from the Korea Advanced Institute of Science and Technology (KAIST), Daejeon, South Korea, in 2021, with a thesis on CMOS wideband power amplifier and low-noise amplifier design. She is currently pursuing the Ph.D. degree at the RF and Electromagnetics Group, University of Colorado at Boulder, Boulder, CO, USA.

Her current research is on the development of noninvasive internal body temperature sensors.

Gabriel Santamaria Botello (Member, IEEE) received the B.Sc. degree in electrical engineering from the University of Carabobo, Valencia, Venezuela, in 2014, and the Ph.D. degree from the Group of Radio frequency, Electromagnetism, Microwaves, and Antennas, Charles III University of Madrid (UC3M), Madrid, Spain, in January 2021, with a focus on the theoretical analysis of terahertz (THz)-to-optical upconversion via resonant electro-optics techniques for high-sensitivity THz radiometry.

From 2021 to 2023, he was a Research Associate at the University of Colorado, Boulder, CO, USA, where he researched RF field sensing using Rydberg atoms and noninvasive internal body temperature measurements using microwave radiometry. He is currently an Assistant Professor with the Colorado School of Mines, Golden, CO, USA.

Robert Streeter (Member, IEEE) received the B.S. degree in electrical and computer engineering and the M.S. degree in electrical engineering from the University of Wyoming, Laramie, Wyoming, in 2011 and 2013, respectively, and the Ph.D. degree in electrical engineering from the University of Colorado, Boulder, CO, USA, in 2023, with a focus on microwave radiometry for medical applications.

He has worked on Unmanned Aircraft Systems (UAS) decision-making algorithms and test protocols for the U.S. Air Force Academy, Colorado Springs, CO, USA, as a Research Engineer; LMR and IP system design, deployment, and maintenance for public and private entities with Ryan Electronics, Inc, Saratoga, WY, USA. He was a winter-over Research Associate at the Amundsen-Scott South Pole Station (under employment by Leidos for the Antarctic Support Contract, which is operated by the NSF), South Pole, Antarctica. He is currently the Site Supervisor at Summit Research Station in central Greenland. His research interests are in engineering education and interdisciplinary, including medical applications of electrical engineering principles.

Zoya Popović (Fellow, IEEE) received the Dipl.-Ing. degree from the University of Belgrade, Belgrade, Serbia, in 1985, and the Ph.D. degree from Caltech, Pasadena, CA, USA, in 1990.

She was a Visiting Professor with the Technical University of Munich, Munich, Germany, from 2001 to 2003, and ISAE, Toulouse, France, in 2014. She was the Chair of Excellence at Carlos III University, Madrid, Spain, from 2018 to 2019. She is currently a Distinguished Professor and the Lockheed Martin Endowed Chair in Electrical Engineering at the University of Colorado at Boulder, Boulder, CO, USA. She has graduated over 70 Ph.D. students and currently advises 18 doctoral students. Her research interests are in high-efficiency power amplifiers and transmitters, microwave and millimeter-wave high-performance circuits for communications and radar, medical applications of microwaves, quantum sensing and metrology, and wireless powering.

Dr. Popović was elected as a member of the National Academy of Engineering in 2022. She was a recipient of two IEEE MTT Microwave Prizes for best journal articles, the White House NSF Presidential Faculty Fellow Award, the URSI Issac Koga Gold Medal, the ASEE/HP Terman Medal, and the German Alexander von Humboldt Research Award. She was elected as a Foreign Member of the Serbian Academy of Sciences and Arts in 2006. She was named IEEE MTT Distinguished Educator in 2013 and the University of Colorado Distinguished Research Lecturer in 2015.